Experimental and theoretical insights into borohydride-based reduction induced metal interdiffusion in Fe-oxide@$NiCo_2O_4$ for enhanced oxygen evolution

Yongcheol Jo,[a] Sangeun Cho,[a] Jiwoo Seo,[a] Abu Talha Aqueel Ahmed,[a] Chi Ho Lee,[b] Jun Ho Seok,[b] Bo Hou,[c,†] Supriya A. Patil,[d] Youngsin Park,[e] Nabeen K. Shrestha,[a,] Sang Uck Lee,[c,*] Hyungsang Kim,[a,*] and Hyunsik Im[a,*]*

[a] Division of Physics and Semiconductor Science, Dongguk University, Seoul 04620, South Korea.

[b] Department of Applied Chemistry, Center for Bionano Intelligence Education and Research, Hanyang University, Ansan 15588, South Korea

[c] Department of Engineering Science, University of Oxford, Parks Road, OX1 3PJ, United Kingdom.

[d] Department of Nanotechnology and Advanced Materials Engineering, Sejong University, Seoul 05006, Republic of Korea.

[e] School of Natural Science, UNIST, Ulsan 44919, Korea

KEYWORDS: Bi-layered $Fe_3O_4/NiCo_2O_4$, chemical reduction, metal-interdiffusion, electrocatalytic water-splitting, oxygen evolution reaction (OER)

ABSTRACT: Oxygen evolution reaction (OER) plays a key role in determining the performance of overall water-splitting, while a core technological consideration is the development of cost-effective, efficient, and durable catalysts. Here, we demonstrate a robust reduced Fe-oxide@$NiCo_2O_4$ bi-layered non-precious metal oxide composite as a highly efficient OER catalyst in an alkaline medium. A bi-layered oxide composite film with an interconnected nanoflake morphology (Fe_2O_3@$NiCo_2O_4$) is reduced in an aqueous $NaBH_4$ solution, which results in a moss-like Fe_3O_4@$NiCo_2O_4$ (reduced Fe-oxide@$NiCo_2O_4$; rFNCO) nanostructured film with an enhanced electrochemical surface area. The rFNCO film demonstrates an outstanding OER activity with an extraordinary low overpotential of 189 mV at 10 mA cm^{-2} (246 mV at 100 mA cm^{-2}) and a remarkably small Tafel slope of 32 mV dec^{-1}. The film also has an excellent durability for more than 50 hours of continuous operation, even at 100 mA cm^{-2}. Furthermore, density functional theory calculations suggest that the unintentionally *in-situ* doped Ni during the reduction reaction possibly improves the OER performance of the rFNCO catalyst shifting *d*-band centers of both Fe and Ni active sites.

1. Introduction

To fulfil the ever-increasing global energy demand while simultaneously considering the environmental impact and the limited availability of natural resources, a wide variety of efficient and cost-effective energy conversion and storage devices have been devised and tested.[1-3] Of these devices, hydrogen generation from electrochemical water-splitting is particularly promising because of its unique advantages, including resource abundance, a CO_2-free process, and the potential for using renewable energy technologies as a sustainable power source. Two types of reactions occur in the electrolysis of water: the oxygen evolution reaction

(OER) at the anode and the hydrogen evolution reaction (HER) at the cathode.[4] Because the generation of oxygen kinetically requires the transfer of four electrons, a higher overpotential is needed for the OER.[5] Therefore, to produce highly efficient water-splitting electrolyzers, the design of low-overpotential-demanding OER catalysts is crucial. Toward this endeavor, iridium oxide (IrO_2), ruthenium oxide (RuO_2), and platinum (Pt) have been widely used as highly efficient electro-catalytic water splitting electrodes.[6,7] However, despite their high catalytic performance, the scarcity and high cost of the raw materials have limited their commercial application in water electrolysis. As a result, significant efforts have been made to replace these noble metal-based electrocatalysts with cost-effective and non-precious metal-based electrodes.

Over the past few years, metal hydroxides/oxides have been investigated as cost-effective and efficient OER and HER catalysts.[8-15] To achieve high electrocatalytic performance, it is important to design an electrode material with a large surface area having a high number of electrochemically active sites and high electrical conductivity.[6,13] Bulk materials (in powder form) are structurally unstable and suffer from poor electrochemical performance due to their limited surface area, circumscribing the number of active reaction sites.[10,16,17] Therefore, a general strategy for producing suitable electrodes is the growth of binder-free nanostructured active materials, such as nanotubes, nanosheets, hollow structures, and nanowires on mesoporous substrates.[18-27] The use of these materials can increase the electrochemically active surface area (ECSA) and electrical conductivity compared to their bulk counterpart, thus enhancing their electrocatalytic and electrochemical properties.

In this work, we demonstrate the direct growth of a non-precious metal-based oxide composite by reducing bi-layered oxide nanosheets of Fe_3O_4 and $NiCo_2O_4$ (*viz*. reduced Fe-oxide@$NiCo_2O_4$ denoted as rFNCO). The rFNCO composite electrode was prepared on Ni foam via electrodeposition, followed by annealing and a reduction reaction. A well-defined

mesoporous rFNCO electrode with a moss-like nanostructured surface was achieved, exhibiting outstanding water-splitting performance in an aqueous alkaline electrolyte. It exhibits an ultra-low OER overpotential of 189 mV at 10 mA cm^{-2} (246 mV at 100 mA cm^{-2}) with a very small Tafel slope of 32 mV dec^{-1}. Also, the electrode shows excellent long-term electrochemical stability even at a high current density of 100 mA cm^{-2}. Moreover, density functional theory (DFT) calculations were performed to further understand the improved OER performance. This catalytic material is particularly advantageous due to its structural integrity, high aspect ratio, easy accessibility, and rich active sites.

2. Experimental

2.1. Material Synthesis

Moss-like rFNCO electrodes were fabricated on a Ni foam substrate sequentially using the following synthesis process: (i) electrodeposition of the $NiCo_2O_4$ (NCO) bottom layer on the Ni foam substrate, (ii) electrodeposition of the top Fe_2O_3 layer on the NCO layer followed by thermal annealing, and finally (iii) chemical reduction to produce rFNCO (Fig. 1). For electrodeposition of the bi-layered metal oxide composite film, Ni foam was used as the working electrode (WE) while a Pt wire served as the counter electrode (CE) and a saturated calomel electrode (SCE) was employed as the reference electrode (RE). Before electrodeposition, the Ni foam substrate, with an area of 1×5 cm^2, was consecutively cleaned via sonication with 3 M HCl, acetone, ethanol, and deionized water to remove the native oxide layer and surface impurities.

Thin bi-layered metal oxide composite films were potentiostatically electrodeposited in an aqueous bath containing different molar concentrations of $FeCl_2{\cdot}4H_2O$ and different molar ratios of $Ni(NO_3)_2{\cdot}6H_2O$ and $Co(NO_3)_2{\cdot}6H_2O$ precursors. NCO was first electrodeposited under a constant potential of −1.0 V (vs SCE). Four molar concentration ratios of $Ni(NO_3)_2$:$Co(NO_3)_2$

(1:2, 1:1, 2:1, and 4:1) were examined, and a ratio of 2:1 was found to be the optimal selection, with the lowest overpotential and Tafel slope (Fig. S1). The top Fe_2O_3 layer was then fabricated in a bath containing a $FeCl_2{\cdot}4H_2O$ precursor under a constant potential of −1.0 V (vs SCE). The top Fe_2O_3 layer was also optimized by varying the $FeCl_2$ molar concentration (5, 15, 30, 45, and 60 mM), and the molar concentration of 45 mM exhibited the best performance. The bi-layered $Fe_2O_3/NiCo_2O_4$ (FNCO) film was then rinsed with ethanol and deionized water and dried at 60 °C for 12 hours and annealed at 200 °C for 2 hours with a ramping rate of 1 °C/min. Finally, to enhance the electrochemical activity, the FNCO film was soaked in a 0.1 M aqueous $NaBH_4$ solution, for 30 minutes, to induce a reduction reaction and obtain the final rFNCO film.

2.2. Characterization methods

The morphologies and chemical compositions of the electrode films produced at each synthesis step were investigated using field emission scanning electron microscopy (FE-SEM) coupled with energy-dispersive X-ray spectroscopy (EDS) and an image-mapping accessory. The crystal structure and composition of the films were determined using high-resolution transmission electron microscopy (HR-TEM), high-angle annular dark (HAADF) scanning transmission electron microscope (STEM), selected area electron diffraction (SEAD), and HAADF-STEM EDS elemental mapping. Binding states were investigated via X-ray photoelectron spectroscopy (XPS).

2.3. Electrochemical measurements and analysis

The electrocatalytic OER performance of the electrodes was evaluated using linear sweep voltammetry (LSV), electrochemical impedance spectroscopy (EIS) and cyclic voltammetry (CV). Electrochemical measurements were performed in a conventional three-electrode cell,

where a platinum wire served as the CE, the proposed moss-like rFNCO electrode was used as the WE, and an SCE was employed as the RE. An aqueous 1 M KOH solution was used as the electrolyte.

3. Results and discussion

3.1. The structural and morphological properties of the catalyst films

Figures 2a-d show top-view FE-SEM images of the Ni foam substrate, NCO, FNCO, and rFNCO, respectively. The substrate was fully covered by the electrochemically active materials after each deposition and reduction step (Figs. 2b-d). While the NCO and FNCO electrodes consisted of similarly shaped interconnected nanosheets, the rFNCO electrode demonstrated moss-like aggregates of nanoparticles. The dramatic morphological change from nanosheets to aggregated nanoparticles is related to the hydroxyl species that are produced by hydrolysis of $NaBH_4$ solution used in the chemical reduction of FNCO.[24] This is more discussed in a following section with the XPS results. Moss-like aggregates began to form on the edges of the nanosheet, eventually covering surface of the nanosheet (Fig. S2). Moreover, not only on the surface, but their presence all over the film and NCO base-nanosheets structures beneath them are confirmed via FIB cross-section TEM and EDS (Figs. S3 and S4). Based on the EDS analysis, the atomic Co:Ni ratio in NCO, FNCO, and rFNCO were determined to be 1:11.73; 1:10.50, and 1:24, respectively (Table S1). However, due to the thin-film deposits, penetration of the X-ray probe could have reached the NF substrate. Thus, the measured Ni content for the samples may be higher than the actual values.

The formation of a nanoscale morphology was revealed by electron microscopy. Figures 3a-c present TEM images of the NCO, FNCO, and rFNCO samples, respectively. Interestingly, Fig. 3a shows that the nanosheets are made up of numerous interconnected nanoparticles with a slightly crumpled surface at the edge of the sheet (marked with an arrow), which can also be

observed in the FE-SEM image for the NCO sample (Fig. 2b). Even after the addition of Fe_2O_3, the nanosheet morphology was maintained, but the crumpled edges of these nanosheets became wider in the FNCO sample (Fig. 3b, marked with arrows). Also, the TEM image of the rFNCO sample (Fig. 3c) shows aggregated nanoparticles, which is consistent with the aggregated nanoparticles observed in the FE-SEM image (Fig. 2d). Moreover, HAADF-STEM elemental mapping results confirm uniform distributions of the constituents (Fig. S4). After the reduction of $NaBH_4$, a small amount of boron is clearly detected in the EDX and XPS spectra of the rFNCO electrode.

3.2. Crystal phase and chemical composition analysis

Crystallinity and microstructure of the as-prepared samples were studied via comprehensive electron microscopy characterizations, as shown in Figs. 3d-g. The NCO sample (Fig. 3d) exhibits lattice fringe distances (*d*) of 0.15 and 0.21 nm, which are associated with the (511) and (400) planes of $NiCo_2O_4$ (JCPDS 73-1702), respectively. The FNCO sample (Fig. 3e) has a *d* of 0.30 (indicated by the white box) and 0.27 nm (blue box), corresponding to the (220) plane of NiCo2O4 (JCPDS 20-0781) and the (104) plane of Fe_2O_3 (JCPDS 89-0599), respectively. Finally, the HRTEM image of the rFNCO sample presented in Fig. 3f reveals *d* of 0.26 nm, corresponding to the (311) plane of Fe_3O_4 (JCPDS 89-0951). The transformation from Fe_2O_3 to Fe_3O_4 phase is likely due to the chemical reduction of Fe^{3+} in Fe_2O_3 by $NaBH_4$. As a result, the Fe_3O_4 phase was detected on the rFNCO surface instead of Fe_2O_3. However, no $NiCo_2O_4$ phase is resolved in the HR-TEM image of rFNCO, possibly due to the poor crystallinity of the as-deposited NCO layer and the amorphous phase generated during the reduction process. Diffused SEAD ring patterns and dot patterns can be observed in Fig. 3g, which indicates the coexistence of polycrystalline and amorphous phases in NCO.[28] Figure 3h presents the concentric SEAD ring patterns for the FNCO sample, which can be attributed to

the coexistence of $NiCo_2O_4$ (JCPDS 20-0781) and Fe_2O_3 (JCPDS 89-0599) phases. This is in good agreement with the HR-TEM image of FNCO, as displayed in Fig. 3e. Overall, these microscopy results suggest that the $NiCo_2O_4$ flakes are covered by the Fe_2O_3 nanostructures. In addition, no significant lattice expansion can be resolved, implying that the Fe-based compound is not intercalated with the $NiCo_2O_4$. Moreover, based on the TEM, HR-TEM and SEAD analyses, we could conclude that the as-prepared NCO film is polycrystalline in nature before the Fe_2O_3 coating but transformed into the amorphous phase during the chemical reduction process. Also, it is worth noting from Figs. S3b and S4c that Ni-species from the underlying nanosheets can be doped into Fe_3O_4 during the reduction reaction. DFT calculations reveal that this presumption of Ni-doping can explain the remarkably improved OER performance after the reduction, and the point will be discussed in detail in a subsequent section.

The elemental composition and oxidation states of the as-prepared FNCO and the rFNCO electrodes were confirmed by XPS analysis. As shown in Fig. 4a, the FNCO electrode has three Fe $2p^{3/2}$ peaks at 719.2, 714.2, and 711.4 eV, which corresponded to the satellite, Fe^{3+} and Fe^{2+} oxidation states, respectively.[29-31] On the other hand, the rFNCO electrode displays shifted peaks at 717.4, 713.9, and 711.0 eV. An additional peak at 707.1 eV (marked with the thick arrow) corresponds to the metallic binding state of Fe^0. After the reduction process, the intensity of the binding peaks also decreased. The observation of negatively shifted peaks and the metallic binding state for the rFNCO electrode indicates that the film had been successfully reduced and would likely become conductive after the chemical reduction reaction. This would electronically bridge the rFNCO and the corresponding catalytically active M-OOH formed, as a result of the anodic bias during the OER, with the NF substrate. Consequently, the charge transfer resistance between the electrode and the electrolyte is reduced, resulting in enhanced OER catalytic activity.

The $NaBH_4$-based reduction is a result of the spontaneous release of H_2 from the exothermic reaction between $NaBH_4$ and H_2O:[32,33]

$$NaBH_4 + 4H_2O \rightarrow NaB(OH)_4 + 4H_2$$

$$3Fe_2O_3 + H_2 \rightarrow 2Fe_3O_4 + H_2O$$

Further, because the intermediate wüstite oxide, $Fe_{1-x}O$ is not stable below 570 °C, Fe_3O_4 can be reduced partially as metallic iron (Fe), which can be described as follows:[33]

$$Fe_3O_4 + 4H_2 \rightarrow 3Fe + 4H_2O.$$

The reduction of Fe_2O_3 was also confirmed by the O 1*s* spectra (Fig. 4b). For the FNCO sample, the spectrum was deconvoluted into three binding peaks at 532.7, 531.5, and 530.2 eV which correspond to carbon-related or surface-absorbed water molecules (O1), lattice FeOH or absorbed hydroxyl (O2), and oxygen atoms bound to metals (O3), respectively.[34] After the reduction process, the metal-binding peak O3 decreased significantly, whereas the other two peaks at higher energies increased, especially O2. This finding is consistent with the presence of the metallic binding state Fe^0 observed for the rFNCO. In addition, in line with the above hydrolysis reaction of $NaBH_4$, the stronger hydroxyl species-related peak (O2) in the rFNCO sample is possibly due to the residual $NaB(OH)_4$ that formed during the hydrolysis of $NaBH_4$, suggesting that hydroxyl species are produced during the reduction process. Xu et al. demonstrated that the hydroxyl ions in a reaction solution regulate Fe_3O_4 morphology.[24] Based on the first principle, they calculated the adsorption energies of OH^- on different crystal planes of Fe_3O_4 and showed that, when the influence of OH^- adsorption on specific crystal planes is low, isotropic spherical Fe_3O_4 forms. In the present study, the hydrolysis of $NaBH_4$ that occurs during the chemical reduction of FNCO produces a weak $NaB(OH)_4$ base, resulting in the low concentration of OH^- species. Under this low OH^- concentration, a similar morphological evolution occurs, leading to the formation of moss-like aggregates of nanoparticles.

3.3. Evaluation of the electrocatalytic activity and stability

The electrocatalytic OER activity of the electrodes, including bare nickel foam (NF), were evaluated using LSV at a scan rate of 10 mV s^{-1} (Fig. 5a). The bare NF electrode exhibits the weakest catalytic activity, requiring a high overpotential of 318 mV at 10 mA cm^{-2}. The electrocatalytic water-splitting performance of the other samples is compared in terms of their overpotential in delivering benchmark current densities of 10, 50, and 100 mA cm^{-2} (Fig. 5 b). During the LSV measurements, the Fe-oxide and FNCO electrodes produced a current density of 10 mA cm^{-2} at an overpotential of 243 mV and 219 mV, respectively. Notably, the rFNCO electrode shows that a remarkably low overpotential of only 189 mV is required to deliver a current density of 10 mA cm^{-2}. The rFNCO electrode also exhibits a very low overpotential of 246 mV even at a very high current density of 100 mA cm^{-2}. It is worth noting that the catalytic OER activity achieved by the rFNCO electrode is comparable or even superior to that of the recently reported state-of-the-art non-precious metal oxide-based electrocatalysts (Fig. 5c).[35-44] Furthermore, the intrinsic activity of the samples was assessed by normalizing the geometrical current density using the corresponding ECSA,[26] as shown in ECSA-based LSV curves (Fig. S7). The normalized LSV curves revealed that the intrinsic OER catalytic activity of the samples followed the same order of rFNCO> FNCO> NCO, as observed in the geometrical area-based voltammograms.

Tafel slopes were obtained from the LSV plots of the catalysts to assess the OER kinetics (Fig. 5d). The Tafel slope of the rFNCO electrode is 32 mV dec^{-1}, which is smaller than those of the NF (71 mV dec^{-1}), NCO (45 mV dec^{-1}), Fe-oxide (36 mV dec^{-1}), and FNCO (43 mV dec^{-1}) electrodes. The Tafel slope is superior compared to those of the state-of-the-art commercial RuO_2 (72 mV dec^{-1}) and MOF-based (42 mV dec^{-1}) electrodes.[7,36] The very small Tafel slope of the rFNCO/NF electrode indicates rapid electron/mass transfer between the electrode and the electrolyte during the OER, confirming its superior OER kinetics.

Interestingly, the Tafel slopes of the rFNCO and Fe-oxide electrodes remained steep even at high currents. This is because the morphology of rFNCO and Fe-oxide allows for the effective release of bubbles from the electrodes during O_2 evolution.

EIS measurements were carried out to further elucidate the kinetics of the electrocatalytic OER reaction at an AC excitation potential of 10 mV and frequencies ranging from 0.1 Hz to 10 kHz. The EIS spectra of the electrodes are presented in Fig. 5e. The obtained Nyquist plots were fitted using a simple equivalent circuit (see the inset of Fig. 5e), which is denoted by the solid lines. Details of the impedance parameters extracted from the fitting of the Nyquist plots are provided in Table S2. The R_s represents a combination of the bulk electrolyte resistance, the internal resistance of the substrate, including contact with the current collector, and other contact resistances.[45-47] The semi-circle is attributed to the charge transfer resistance (R_{ct}) whereas the straight line is assigned to Warburg impedance (W) which is representative of the diffusion behaviour of an electrode material for electroactive species.[48] The NCO electrode has R_s and R_{ct} of 0.93 Ω and 0.17 Ω, respectively. The FNCO electrode has lower values of 0.84 Ω and 0.16 Ω, respectively, suggesting that the intrinsic and charge transfer resistance of the electrode is reduced after FeO deposition. After the reduction process, it was found that the electron/ion transport became more efficient, with a further reduction in R_{ct} to 0.11 Ω for the rFNCO electrode. Thus, the R_{ct} for the rFNCO electrode is improved by more than 30% compared with that of the NCO and FNCO electrodes. This is associated with the synergistic effects of extensive contact with the electrolyte and the shorter ion-diffusion pathways resulting from the moss-like aggregated nanoparticle surface of the rFNCO containing Fe^0. Also, the slope of the Warburg element in low-frequency region increased dramatically after the reduction process (NCO < FNCO < rFNCO). The rapid and efficient electron/ion transport at the electrode/electrolyte interface is the direct result of many oxygen vacancies produced by the reduction process and the moss-like morphology of the rFNCO. These factors facilitate the

transport of the electrons and OER active species such as OH^-, promote their interaction with the catalytically active sites and remove bubbles on the surface effectively, thus enhancing OER reaction kinetics.[9,47]

To confirm the reproducibility of the observed OER performance, several rFNCO electrode films were fabricated under the same conditions and their OER properties were assessed. The average overpotential for these films was 198 mV at a current density of 10 mA cm^{-2}, with an acceptable standard deviation of ± 8 mV. Similarly, the average Tafel slope was 37 mV dec^{-1} ± 4 mV dec^{-1} (Fig. S5).

To comprehensively understand the effect of the electrode kinetics, as indicated by the Tafel slopes and EIS spectra on the electrochemical reaction at the electrolyte/electrode interface, the ECSA of each electrode was evaluated by determining its electrochemical double-layer capacitance (EDLC; C_{dl}).[49] (Fig S6) As shown in Fig. 6a, the estimated ECSA for the NCO, FNCO, and rFNCO electrodes was 365.0, 537.5, and 1222.5 cm^2, respectively, showing that the rFNCO electrode was significantly more electrochemically active than the other electrodes. This suggests that the reduction process resulted in a high density of electrochemically active sites on the FNCO electrode. Consequently, the kinetic activity of the rFNCO electrocatalyst was much higher than those of the other electrodes.

Figure 7a shows the results of stability for the rFNCO electrode based on a chronopotentiometry test. Constant current densities of 10, 50, and 100 mA cm^{-2} were applied for 20 hours each and the corresponding overpotential was measured. The rFNCO electrode shows excellent stability with very little fluctuation (< 4 mV, ~ 1 %) even at high current densities. Figure 7b presents the LSV curves of the rFNCO electrode before and after stability testing. The measured LSV curves are almost identical, thus confirming its electrochemical stability. The measured electrochemical stability of the FNCO electrode at various current

densities is presented in Fig. S8 (Supplementary Information), revealing a relatively poor stability particularly at a high current bias.

The SEM images of rFNCO both before and after the stability test are shown in Fig. 7c and Fig. S9. After a long-term stability test, bulky submicron-sized agglomerates formed on the surface. To identify the origin of these agglomerates, the chemical composition of the electrode after the stability test was investigated using SEM-EDS. As shown in the elemental mapping images, the main elemental components of the agglomerates are potassium (K) and oxygen (O), which originate from the KOH electrolyte. In addition, after the long-term stability test, the metallic Fe^0 peak disappears from the Fe 2p spectrum but the O3 peak (associated with Fe-O binding) in the O 1s spectrum increases, indicating that the metallic Fe was oxidized (Fig. S10 in the Supplementary Information). Although electrolyte-associated agglomerates were detected during the stability test, the rFNCO electrode still exhibited remarkable electrochemical stability, suggesting that the agglomerates cover only a small portion of the electrode and there is a negligible phase transition. The unique moss-like morphology of the rFNCO is also considered as a critical factor contributing to the excellent stability because the generated gas bubbles can be effectively released from the electrode, thus maintaining the initially existing high number of electrochemically active sites. The measured stability of various catalysts including our sample is presented in Table S3 in the Supplementary Information.

3.4. Computational calculations

Furthermore, we also performed DFT calculations to gain further insights into the origin of the OER electrocatalytic activity on the Ni-doped Fe_3O_4 structure. For the investigation of the Ni incorporation effect on the improved OER performance, we preferentially designed reasonable Ni doped Fe_3O_4 bulk and surface structures (Figs S11, designed structures are

described in the Supplementary Information) based on the experimental TEM-EDS results on the surface of the rFNCO composite (Fig S3b). Given the well-established pure and doped structure, we systematically investigated OER activities by overpotential (η^{OER}), using a general free energy diagram (FED) approach (Figs. 12b, S15b, and S16 b) for all possible active sites (Figs. S11c and S12 c,d).[50-52] The calculated FEDs reveal that the $FN_{0.25}O$ structure has a significantly low OER overpotential of 0.41 V outperforming that of $FN_{0.375}O$ (0.61 V) and pure Fe_3O_4 (0.66 V), and it theoretically represents competitive catalytic activity for conventional RuO_2 (0.43 V). Here, the most active FED in Fe_3O_4 clearly shows that the second step of OER (ΔG_2^{OER}) associated with OH* and O* intermediates is a significant uphill reaction (Fig S15b). Therefore, we intensively explored the changes of reaction free energies for all possible Fe sites under the ideal potential to emphasize the importance of ΔG_2^{OER} values (Fig. S16a) and found that the OER overpotentials undoubtedly come from strong OH* and weak O*, which show the linear scaling relationship (Fig. S16b). From these results, one can deduce that the ΔG_2^{OER} plays an important role in determining the OER activity as the potential determining step (PDS). Hence, we systematically investigated ΔG_2^{OER} variations induced by the Ni incorporation ($FN_{0.25}O$ and $FN_{0.375}O$), and identified that the binding strengths of OH* (O*) in the $FN_{0.25}O$ are remarkably lower (higher) than those for a pure system, respectively (Figs. 12a and b). Based on these changed free energies, the results in Fig. S18 also reveal that the difference on ΔG_2^{OER} values under the ideal potential explains the OER activity variations well, which show the improved scaling relationship. This theoretical evaluation implies that the suitable binding of intermediates can make the ΔG_2^{OER} value closer to the ideal potential of 0.402 V in an alkaline media, which leads to the enhanced OER catalytic performance.

The binding strength of intermediates at PDS is strongly correlated with the tendency of valence orbitals of active sites that judge the electron filling of the anti-bonding state near the Fermi level.[53-55] Interestingly, the binding configuration of the OH* is the on-top on the Fe site,

and that of the O* is the bridge on the Fe and Ni sites. Therefore, we focused on the position of the *d*-band center with all-metal sites of the designed pure and doped structures. The partial density of states (PDOS) in Fig. 8c shows that the *d*-band center of Fe (Ni) active sites in the $FN_{0.25}O$ is shifted to a lower (higher) position compared to Fe sites of Fe_3O_4. This theoretical viewpoint implies that the Fe active sites of $FN_{0.25}O$ can have decreased OH* binding strength, whereas the Ni active sites can have increased O* binding strength. Furthermore, the additional electronic results in Fig. S19 reveal that the Fe_3O_4 and $FN_{0.25}O$ structures have metallic properties, which can enhance the catalytic activity, and have the particularly large contribution of metals to frontier energy states around the Fermi level consistent with the active site preference. Consequently, it is worth noticing that the characteristic electronic feature of $FN_{0.25}O$ leads to improving OER catalytic performance by desirably shifting the *d*-band centers of both Fe and Ni active site.

4. Conclusions

The present study demonstrated a simple and scalable electrodeposition process combined with a reduction reaction for the fabrication of NCO, FNCO, and reduced rFNCO electrodes on Ni foam. The $NaBH_4$ reduction reaction reduced Fe_2O_3 and transformed the surface of the FNCO nanosheets into moss-like aggregates of nanoparticles doped with Ni, leading to a significant increase in the ECSA, reducing the number of bubbles on the surface, enhancing conductivity, and subsequently improving the electrochemical OER performance. The DFT calculations showed that the unintentionally *in-situ* doped Ni on Fe_3O_4 can lower the overpotential, improving the OER performance by reducing the required energy in PDS. Experimentally, the optimal rFNCO electrode exhibited a very low overpotential of 189 mV at 10 mA cm^{-2} with an ultra-small Tafel slope of 32 mV dec^{-1}. The rFNCO electrode also exhibited excellent electrochemical stability, with a chronopotentiometric variation of only 4

mV even at a very high current density of 100 mA cm^{-2} for 50 h. Given the present work, key perspectives, such as further development of rFNCO-based nanostructures and the application of other iron compounds for eco-friendly electrochemical water splitting, can be envisioned.

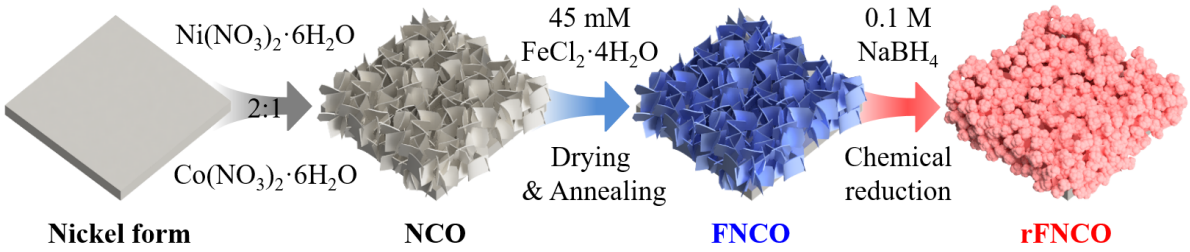

Figure 1. Schematic illustration of the fabrication process for the growth of an rFNCO electrode on Ni foam. The NCO and FNCO films are deposited using a three-electrode system, and a tube furnace is used for annealing.

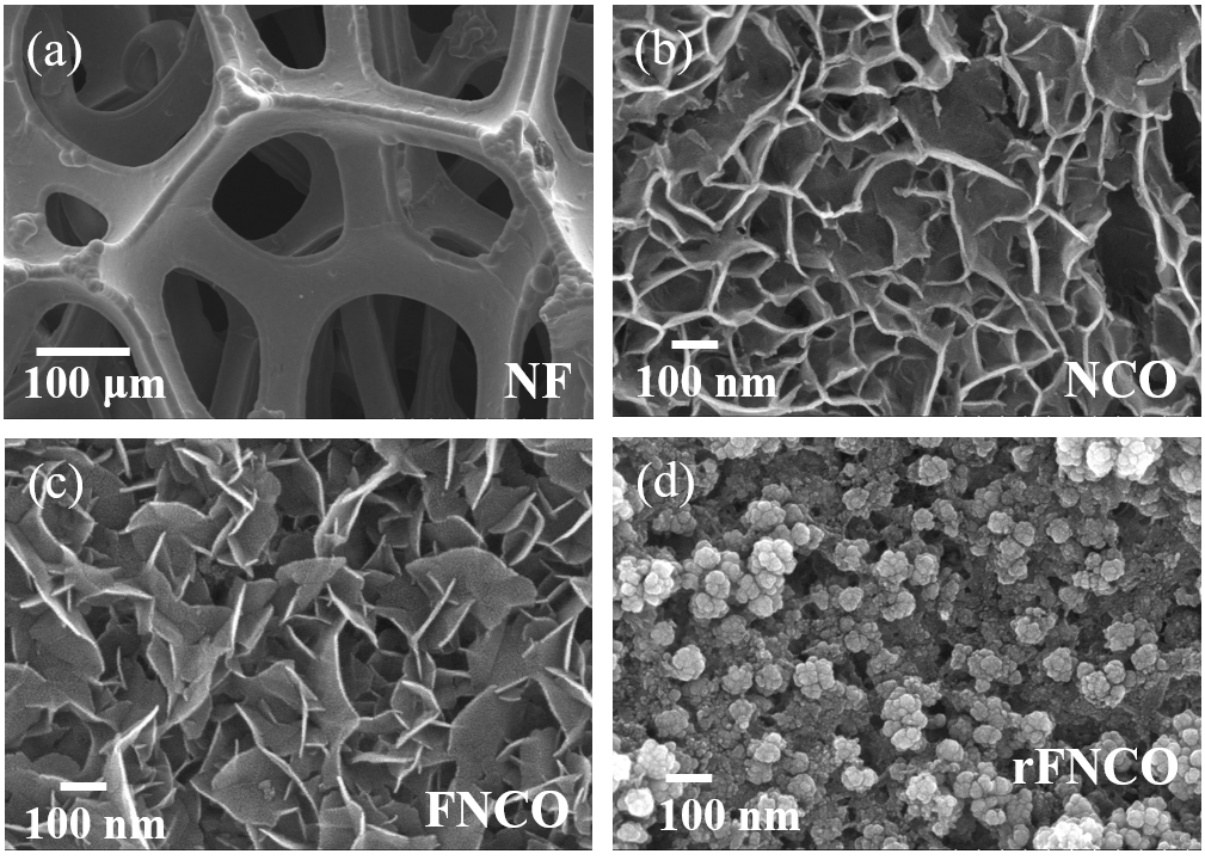

Figure 2. Top FE-SEM views of (a) Ni foam, (b) NCO, (c) FNCO, and (d) rFNCO on a Ni foam substrate. Dramatic morphology transform is observed between FNCO and rFNCO.

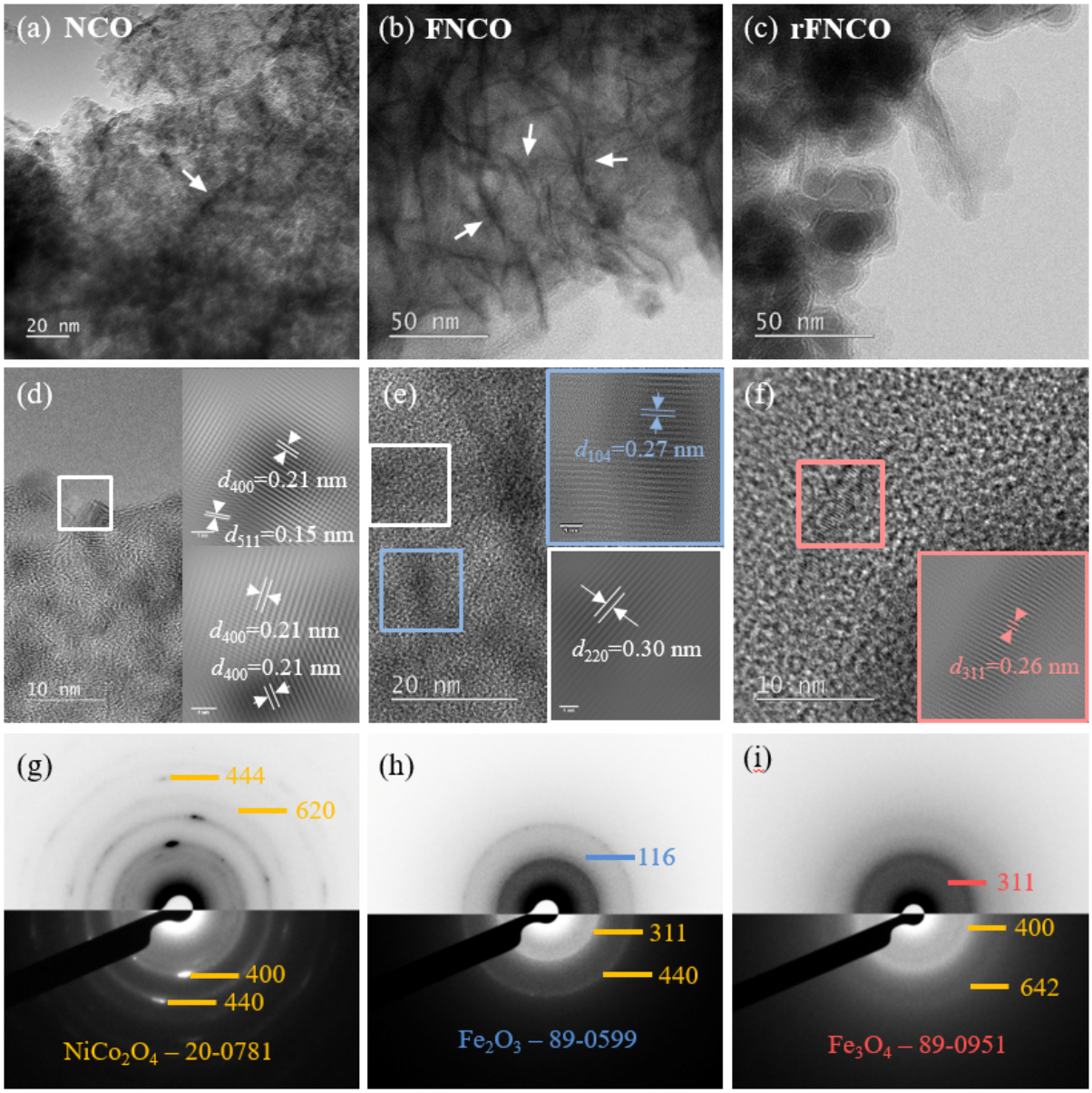

Figure 3. (a-c) Bright-field TEM images, (d-f) HR-TEM images of NCO, FNCO, and rFNCO samples, respectively. White arrows in the bright-field TEM images indicate a crumpled surface at the edges for NCO and FNCO. (g-i) SEAD patterns of NCO, FNCO, and rFNCO samples. White (or orange), Blue, red colours in HR-TEM and SEAD pattern images are associated with NCO, FNCO, and rFNCO, respectively.

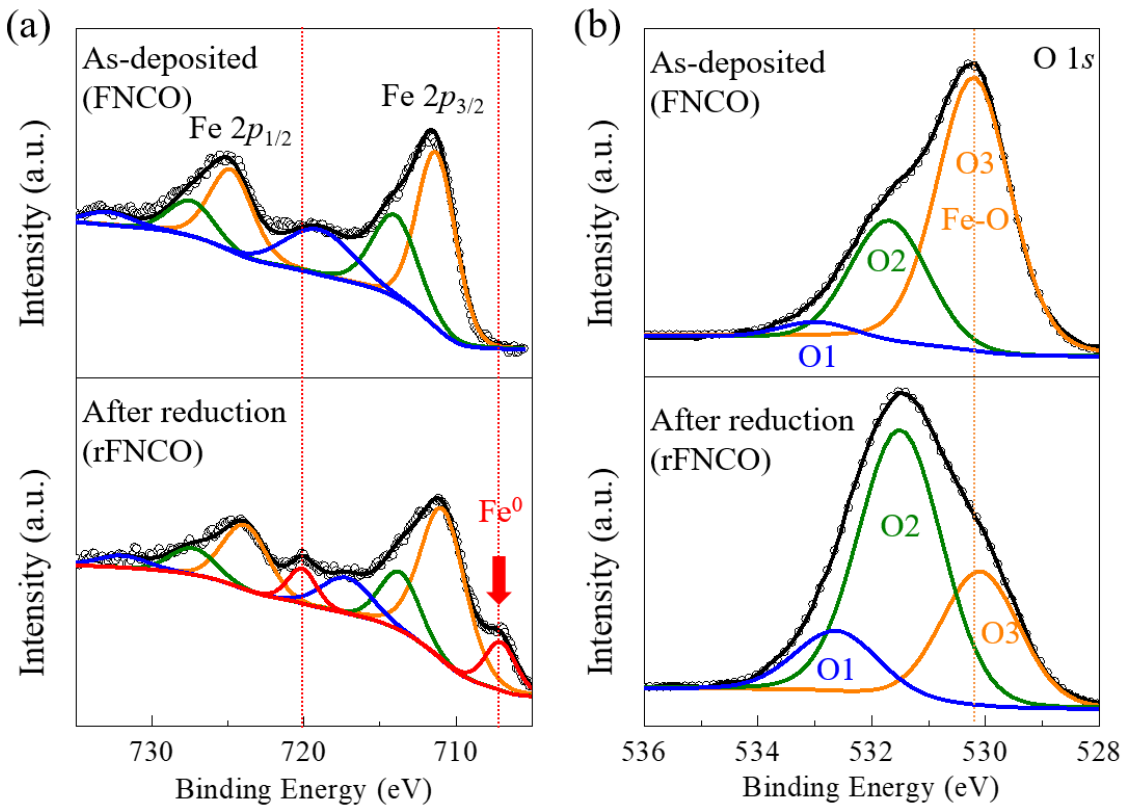

Figure 4. XPS measurements. Core level (a) Fe 2*p* and (b) O 1*s* spectra of the FNCO and rFNCO. The complex XPS spectra are deconvoluted in to several components using the Gaussian-Lorentz curve fitting.

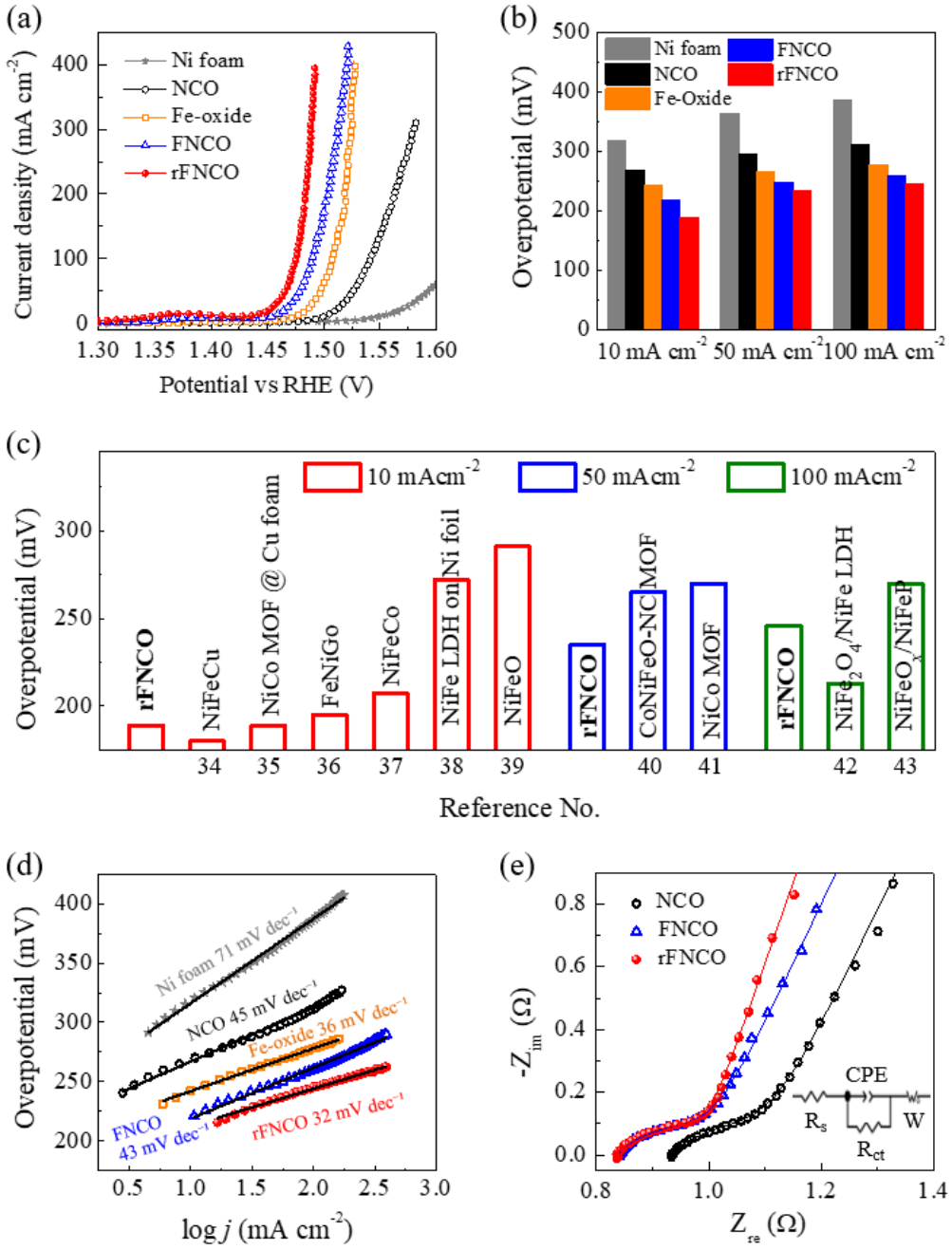

Figure 5. OER catalytic activity of the Ni foam (substrate), Fe-oxide, FNCO, and rFNCO. (a) LSV curves at 10 mV s^{-1}, (b) comparison of the obtained overpotentials at different current densities, (c) comparative electrocatalytic OER performance of our rFNCO catalyst and recently reported state-of-the-art catalysts at various driving current densities, (d) Tafel plots, and (e) Nyquist plots.

(a)

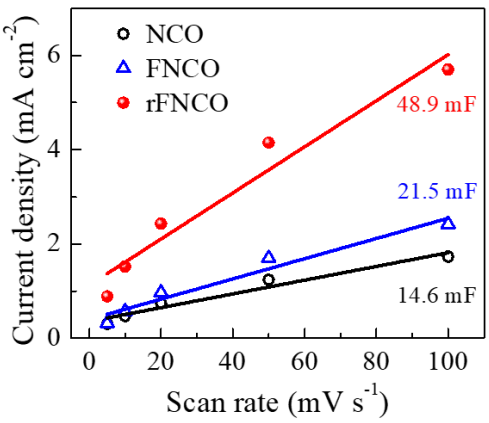

(b)

	NCO	FNCO	rFNCO
ECSA (cm^2)	365.0	537.5	1222.5

Figure 6. (a) Non-faradaic current density obtained from CV curves at 0.22 V as a function of scan rate (mV s^{-1}), and (b) a comparison of the ECSA.

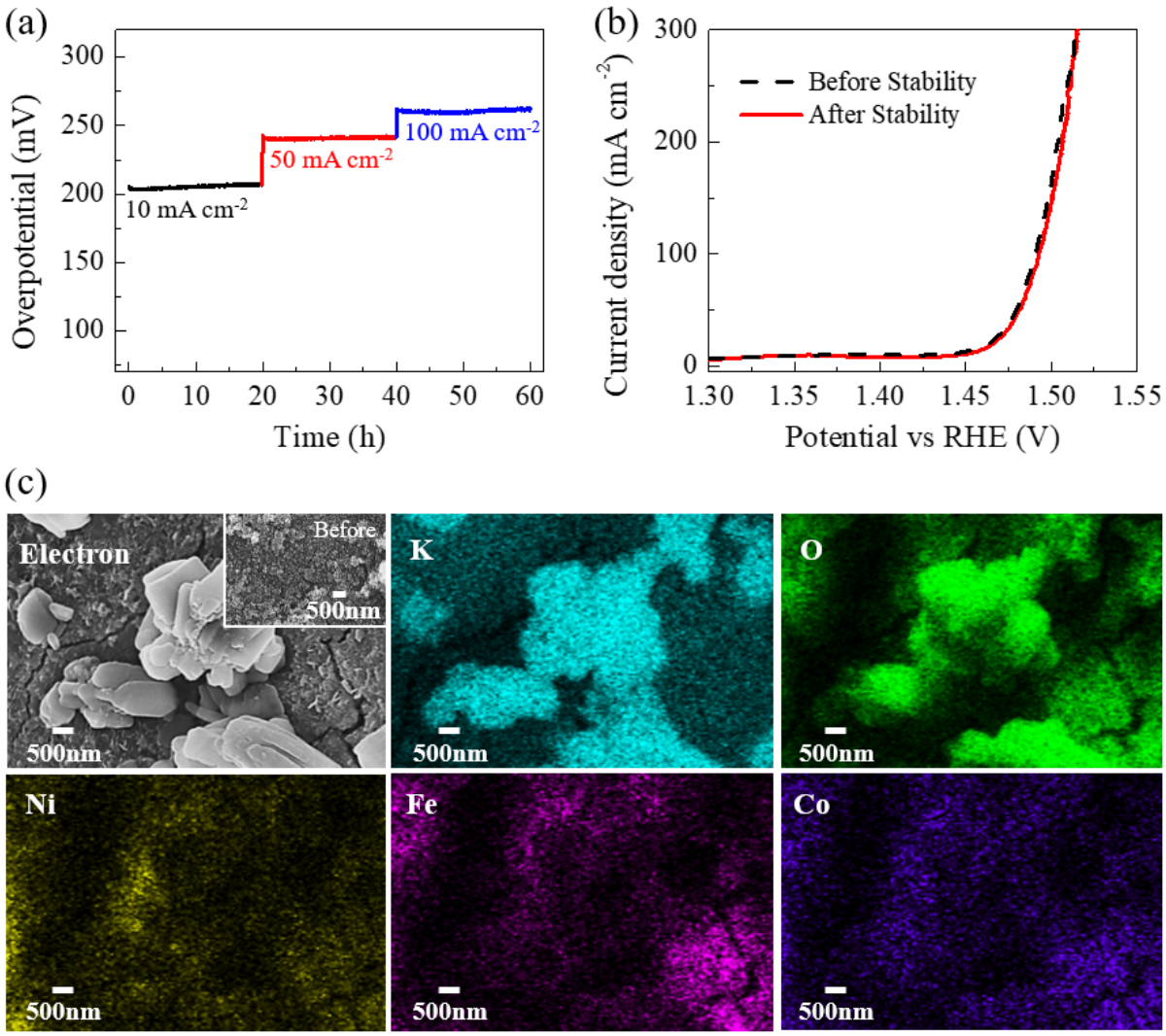

Figure 7. (a) Electrochemical stability of the rFNCO electrode at various current densities, (b) LSV curves for the rFNCO electrode before and after stability testing, and (c) EDS elemental mapping images for the rFNCO electrode after stability testing.

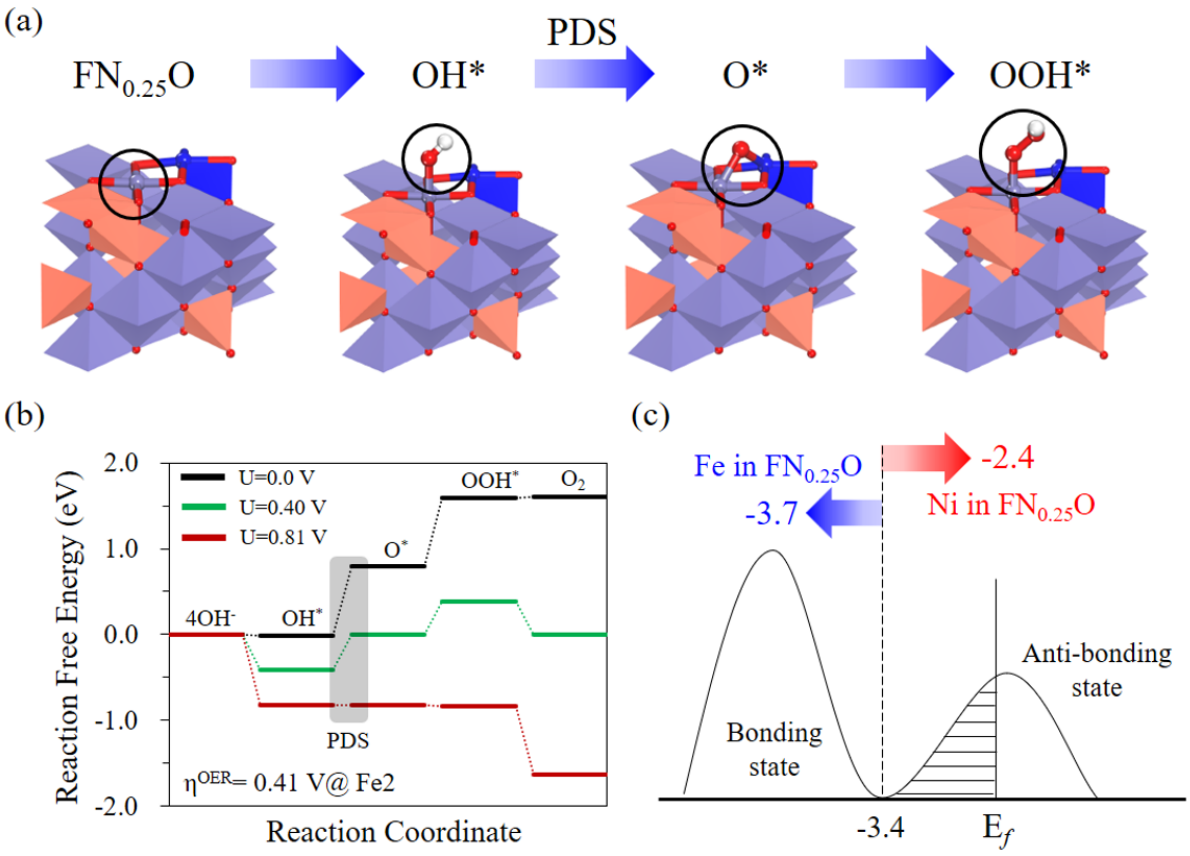

Figure 8. (a) Most active OER mechanistic on the $FN_{0.25}O$ structure and its potential-determining step (PDS). (b) Free energy diagrams on the most active Fe2 active site of $FN_{0.25}O$ for the OER in an alkaline environment. All possible active sites are shown in Fig. S11c. (c) Schemes of *d*-band center variation and anti-bonding state occupation in partial density of states (PDOS) of metal sites in Fe_3O_4 and $FN_{0.25}O$. The black dashed line indicates the standard *d*-band center value of Fe sites in the Fe_3O_4 structure.

ASSOCIATED CONTENT

Supporting Information

Detailed optimization of samples, physical characterizations, electrochemical measurements, and theoretical calculation details and results (PDF). This material is available free of charge via the Internet at http://pubs.acs.org.

AUTHOR INFORMATION

Corresponding Author

Nabeen K. Shrestha - Division of Physics and Semiconductor Science, Dongguk University, Seoul 04620, South Korea; Email: nabeenkshrestha@hotmail.com

Sang Uck Lee - Department of Applied Chemistry, Center for Bionano Intelligence Education and Research, Hanyang University, Ansan 15588, South Korea; Email: sulee@hanyang.ac.kr

Hyungsang Kim - Division of Physics and Semiconductor Science, Dongguk University, Seoul 04620, South Korea; Email: hskim@dongguk.edu

Hyunsik Im - Division of Physics and Semiconductor Science, Dongguk University, Seoul 04620, South Korea; Email: hyunsik7@dongguk.edu

Present Addresses

†School of Physics and Astronomy, Cardiff University, The Parade, Cardiff, Wales, CF24 3AA, United Kingdom.

Author Contributions

Y.J. and S.C. equally contributed to this work as co-first authors. The manuscript was written through contributions of all authors. All authors have given approval to the final version of the manuscript.

Notes

The authors declare no competing financial interest.

ACKNOWLEDGMENT

The authors acknowledge the financial support from the National Research Foundation (NRF) of Korea (Grant nos. 2018R1D1A1B07049046, 2021R1A2B5B01001796, and 2021R1A4A5031805).

REFERENCES

(1) Turner, J. A. Sustainable hydrogen production. *Science* **2004**, 305, 972.

(2) Meyer, T. J. The art of splitting water. *Nature* **2008**, 451, 778-779.

(3) Hussain, A.; Arif, S. M.; Aslam, M. Emerging renewable and sustainable energy technologies: state of the art. *Renew. Sust. Energ. Rev.* **2017**, 71, 12-28.

(4) Wang, J.; Cui, W.; Liu, Q.; Xing, Z.; Asiri, A. M.; Sun, X. Recent progress in cobalt-based heterogeneous catalysts for electrochemical water splitting. *Adv. Mater.* **2016**, 28, 215-230.

(5) You, B.; Sun, Y. Innovative strategies for electrocatalytic water splitting. *Acc. Chem. Res.* **2018**, 51, 1571-1580.

(6) Seitz, L. C.; Dickens, C. F.; Nishio, K.; Hikita, Y.; Montoya, J.; Doyle, A.; Kirk, C.; Vojvodic, A.; Hwang, H. Y.; Norskov, J. K.; Jaramillo, T. F. A highly active and stable $IrO_x/SrIrO_3$ catalyst for the oxygen evolution reaction. *Science* **2016**, 353, 6303.

(7) Liu, M.; Hof, F.; Moro, M.; Valenti, G.; Paolucci, F.; Penicaud, A. Carbon supported noble metal nanoparticles as efficient catalysts for electrochemical water splitting. *Nanoscale* **2020**, 12, 20165.

(8) Inamdar, A. I.; Chavan, H. S.; Hou, B.; Lee, C. H.; Lee, S. U.; Cha, S.; Kim, H.; Im, H. A robust nonprecious CuFe composite as a highly efficient bifunctional catalyst for overall electrochemical water splitting. *Small* **2020**, 16, 1905884.

(9) Ahmed, A. T. A.; Pawar, S. M.; Inamdar, A. I.; Im, H; Kim, H. Fabrication of FeO@$CuCo_2S_4$ multifunctional electrode for ultrahigh-capacity supercapacitors and efficient oxygen evolution reaction. *Int. J. Energy Res.* **2020**, 44, 1798.

(10) Wang, J.; Li, K.; Zhong, H.-X.; Xu, D.; Wang, Z.-L.; Jiang, Z.; Wu, Z.-J.; Zhang, X.-B. Synergistic effect between metal-nitrogen-carbon sheets and NiO nanoparticles for enhanced electrochemical water-oxidation performance. *Angew. Chem. Int. Ed.* **2015**, 54, 10530−10534.

(11) Bae, S.; Kim, J.; Randriamahazaka, H.; Moon, S.; Park, J.; Oh, I. Seamlessly conductive 3D nanoarchitecture of core-shell Ni-Co nanowire network for highly efficient oxygen evolution. *Adv. Energy Mater.* **2017**, 7, 1601492.

(12) Zhu, Y.; Zhang, X.; Koh, K.; Kovarik, L.; Fulton, J. L.; Rosso, K. M.; Gutierrez, O. Y. Inverse iron oxide/metal catalysts from galvanic replacement. *Nat. Commun.* **2020**, 11, 3269.

(13) Chen, P.; Xu, K.; Fang, Z.; Tong, Y.; Wu, J.; Lu, X.; Peng, X.; Ding, H.; Wu, C.; Xie, Y. Metallic Co_4N porous nanowire arrays activated by surface oxidation as electrocatalysts for oxygen evolution reaction. *Angew. Chem. Int. Ed.* **2015**, 54, 14710-14714.

(14) Morales, D. M.; Kazakova, M. A.; Dieckhofer, S.; Selyutin, A. G.; Golubtsov, G. V.; Schuhmann, W.; Masa, J. Trimetallic Mn-Fe-Ni oxide nanoparticles supported on multi-walled carbon nanotubes as high-performance bifunctional ORR/OER electrocatalyst in alkaline media. *Adv. Func. Mater.* **2020**, 30, 1905992.

(15) Dresp, S.; Thanh, T. N.; Klingenhof, M.; Bruckner, S.; Hauke, P.; Strasser, P. Efficient direct seawater electrolyzers using selective alkaline NiFe-LDH as OER catalyst in asymmetric electrolyte feeds. *Energy and Environ. Sci.* **2020**, 13, 1725.

(16) Zhang, Y.; Ma, M.; Yang, J.; Su, H.; Huang, W; Dong, X. Selective synthesis of hierarchical mesoporous spinel $NiCo_2O_4$ for high-performance supercapacitors. *Nanoscale* **2014**, 6, 4303–4308.

(17) Xiao, J.; Yang, S. Sequential crystallization of sea urchin-like bimetallic (Ni, Co) carbonate hydroxide and its morphology conserved conversion to porous $NiCO_2O_4$ spinel for pseudocapacitors. *RSC Adv.* **2011**, 1, 588–595.

(18) Xu, K.; Zou, R.; Li, W.; Liu, Q.; Liu, X.; An, L.; Hu, J. Design and synthesis of 3D interconnected mesoporous $NiCo_2O_4$@$Co_xNi_{1-x}(OH)_2$ core-shell nanosheet arrays large areal capacitance and high rate performance for supercapacitors. *J. Mater. Chem. A* **2014**, 2, 10090–10097.

(19) Ahmed, A. T. A.; Hou, B.; Chavan, H. S.; Jo, Y.; Cho, S.; Kim, J.; Pawar, S. M.; Cha, S. N.; Inamdar, A. I.; Kim, H.; Im, H. Self-assembled nanostructured $CuCo_2O_4$ for electrochemical energy storage and the oxygen evolution reaction via morphology engineering. *Small* **2018**, 14, 1800742-1800751.

(20) Yu, L.; Zhang, G.; Yuan, C.; Lou, X. Hierarchical $NiCo_2O_4$@MnO_2 core-shell heterostructured nanowire arrays on Ni foam as high-performance supercapacitor electrodes. *Chem. Commun.* **2013**, 49, 137–139.

(21) Lv, X.; Li, X.; Yang, C.; Ding, X.; Zhang, Y.; Zheng, Y. –Z.; Li, S.; Sun, X.; Tao, X. Large-size, porous, ultrathin NiCoP nanosheets for efficient electro/photocatalytic water splitting. *Adv. Func. Mater.* **2020**, 30, 1910830.

(22) Manjunatha, C.; Srinivasa, N.; Chaitra, S. K.; Sudeep, M.; Kumar, R. C.; Ashoka, S. Controlled synthesis of nickel sulfide polymorphs: studies on the effect of morphology and crystal structure on OER performance. *Mater. Today Energy* **2020**, 16, 100414.

(23) Shrestha, N. K.; Patil, S. A.; Cho, S.; Jo, Y.; Kim, H.; Im, H. Cu–Fe–NH_2 based metal–organic framework nanosheets via drop-casting for highly efficient oxygen evolution catalysts durable at ultrahigh currents. *J. Mater. Chem. A* **2020**, 8, 24408-24418.

(24) Xu, N.; Yan, H.; Jiao, X.; Jiang, L.; Zhang, R.; Wang, J.; Liu, Z.; Liu, Z.; Gu, Y.; Gang, F.; Wang, X.; Zhao, L.; Sun, X. Effect of OH^- concentration on Fe_3O_4 nanoparticle morphologies supported by first principle calculation. *J. Cryst. Growth* **2020**, 547, 125780.

(25) Lai, Y.; Gao, X.; Zhuang, H.; Huang, J.; Lin, C.; Jiang, L. Designing superhydrophobic porous nanostructures with tunable water adhesion. *Adv. Mater.* **2009**, 21, 3799.

(26) Xu, J.; Liu, Y.; Li, J.; Amorium, I.; Zhang, B.; Xiong, D.; Zhang, N.; Thalluri, S. M.; Sousa, J. P. S.; Liu, L. Hollow cobalt phosphide octahedral pre-catalysts with exceptionally high intrinsic catalytic activity for electro-oxidation of water and methanol. *J. Mater. Chem. A* **2018**, 6, 20646.

(27) Zeng, Y.; Lai, Z.; Han, Y.; Zhang, H.; Xie, S.; Lu, X. Oxygen-vacancy and surface modulation of ultrathin nickel cobaltite nanosheets as a high-energy cathode for advanced Zn-ion batteries. *Adv. Mater*. **2018**, 30, 1802396.

(28) Hou, B.; Parker, D.; Kissling, G. P.; Jones, J. A.; Cherns, D.; Fermin, D. J. Structure and band edge energy of highly luminescent $CdSe_{1-x}Te_x$ alloyed quantum dots. *J. Phys. Chem. C* **2013**, 177, 13.

(29) Zhao, H.; Wang, Y.; Wang, Y.; Cao, T.; Zhao, G. Electro-Fenton oxidation of pesticides with a novel Fe_3O_4@Fe_2O_3/activated carbon aerogel cathode: high activity, wide pH range and catalytic mechanism. *Appl. Catalysis B: Environ.* **2012**, 125, 120.

(30) Lin, T.; Seshadri, G.; Kelber, J. A. A consistent method for quantitative XPS peak analysis of thin oxide films on clean polycrystalline iron surfaces. *Appl. Surf. Sci.* **1997**, 119, 83-92.

(31) Biesinger, M. C.; Payne, B. P.; Grosvenor, A. P.; Lau, L. W. M.; Gerson, A. R.; Smart, R. St. C. Resolving surface chemical states in XPS analysis of first row transition metals, oxides and hydroxides: Cr, Mn, Fe, Co and Ni. *Appl. Surf. Science* **2011**, 257, 2717-2730.

(32) Lai, Q.; Alligier, D.; Aguey-Zinsou, K. –F.; Demirci, U. B. Hydrogen generation from a sodium borohydride-nickel core@shell structure under hydrolytic conditions. *Nanoscale Adv.* **2019**, 1, 2707.

(33) Spreitzer, D.; Schenk, J. Reduction of iron with hydrogen – a review. *Steel Research Int.* **2019**, 90, 1900108.

(34) Eltouny, N.; Ariay, P. A. Competing reactions of selected atmospheric gases on Fe_3O_4 nanoparticles surfaces. *Phys. Chem. Chem. Phys.* **2014**, 16, 23056.

(35) Zhang, P.; Li, L.; Nordlund, D.; Che, H.; Fan, L.; Zhang, B.; Sheng, X.; Daniel, Q.; Sung, L. Dendritic core-shell nickel-iron-copper metal/metal oxide electrode for efficient electrocatalytic water oxidation. *Nat. Commun.* **2018**, 9, 381.

(36) Zhao, S.; Wang, Y.; Dong, J.; He, C.; Yin, H.; An, P.; Zhao, K.; Zhang, X.; Gao, C., Zhang, L.; Lv, J.; Wang, J.; Zhang, J.; Khattak, A. M.; Khan, N. A.; Wei, Z.; Zhang, J.; Liu, S.; Zhao, H.; Tang, Z. Ultrathin metal-organic framework nanosheets for electrocatalytic oxygen evolution. *Nat. Energy* **2016**, 1, 16184.

(37) Long, X.; Li, J.; Xiao, S.; Yan, K.; Wang, Z.; Chen, H.; Yang, S. A strongly coupled graphene and FeNi double hydroxide hybrid as an excellent electrocatalyst for the oxygen evolution reaction. *Angew. Chem. Int. Ed.* **2014**, 53, 7584-7588.

(38) Darband, G. B.; Aliofkhazraei, M.; Hyun, S.; Rouhaghdam, A. S.; Shanmugam, S. Electrodeposition of Ni-Co-Fe mixed sulfide ultrathin nanosheets on Ni nanocones: a low-cost, durable and high performance catalyst for electrochemical water splitting. *Nanoscale* **2019**, 11, 16621.

(39) Kim, S. H.; Park, Y. S.; Kim, C.; Kwon, I. Y.; Lee, J.; Jin, H.; Lee, Y. S.; Choi, S. M.; Kim, Y. Self-assembly of Ni-Fe layered double hydroxide at room temperature for oxygen evolution reaction. *Energy Reports* **2020**, 6, 248.

(40) Yu, M.; Moon, G.; Bill, E.; Tuysuz, H. Optimizing Ni-Fe oxide electrocatalysts for oxygen evolution reaction by using hard templating as a toolbox. *ACS Appl. Eng. Mater.* **2019**, 2, 1199.

(41) Chen, C.; Tuo, Y.; Lu, Q.; Lu, H.; Zhang, S.; Zhou, Y.; Zhang, J.; Liu, Z.; Knag, Z.; Feng, X.; Chen, D. Hierarchical trimetallic Co-Ni-Fe oxides derived from core-shell structured metal-organic frameworks for highly efficient oxygen evolution reaction. *Appl. Catalysis B: Environ.* **2021**, 287, 119953.

(42) Thangasamy, P.; Shanmuganathan, S.; Subramanian, V. A NiCo-MOF nanosheet array based electrocatalyst for the oxygen evolution reaction. *Nanoscale Adv.* **2020**, 2, 2073-2079.

(43) Wu, Z.; Zou, Z.; Huang, J.; Gao, F. $NiFe_2O_4$ nanoparticles/NiFe layered double-hydroixde nanosheet heterostructured array for efficient overall water splitting at large current densities. *ACS Appl. Mater. Interfaces* **2018**, 10, 26283.

(44) Lindstrom, M. L.; Gakhar, R.; Raja, K.; Dhidambaram, D. Facile synthesis of an efficient Ni-Fe-Co based oxygen evolution reaction electrocatalyst. *J. Electrochem. Soc.* **2020**, 167, 046507.

(45) Raja, D. S.; Huang, C.-L.; Chen, Y.-A.; Choi, Y.; Lu, S.-Y. Composition-balanced trimetallic MOFs as ultra-efficient electrocatalysts for oxygen evolution reaction at high current densities. *Applied Catalysis B: Environ.* **2020**, 279, 119375-119388.

(46) Kotz, R.; Carlen, M. Principles and applications of electrochemical capacitors. *Electrochimica Acta* **2000**, 45, 2483-2498.

(47) Mei, B.; Munteshari, O.; Lau, J.; Dunn, B.; Pilon, L. Physical interpretations of Nyquist plots for EDLC electrodes and devices. *J. Phys. Chem. C* **2018**, 122, 194-206.

(48) Ahmed, A. T. A.; Chavan, H. S.; Jo, Y.; Cho, S.; Kim, J.; Pawar, S. M.; Gunjakar, J. L.; Inamdar, A. I.; Kim, H.; Im, H. One-step facile route to copper cobalt sulfide electrodes for supercapacitors with high-rate long-cycle life performance. *J. Alloys and Compd.* **2017**, 724, 744-751.

(49) McCrory, C. C. L.; Jung, S.; Peters, J. C.; Jaramillo, T. F. Benchmarking heterogeneous electrocatalysts for the oxygen evolution reaction. *J. Am. Chem. Soc.* **2013**, 135, 16977-16987.

(50) Norskov, J. K.; Rossmeisl, J.; Logadottir, A.; Lindqvist, L.; Kitchin, J. R.; Bligaard, T.; Jonsson, H. Origin of the overpotential for oxygen reduction at a fuel-cell cathode. *J. Phys. Chem. B* **2004**, 108, 17886-17892.

(51) Man, I. C.; Su, H.; Calle-Vallejo, F.; Hansen, H. A.; Martinez, J. I.; Inoglu, N. G.; Kitchin, J.; Jaramillo, T. F.; Norskov, J. K.; Rossmeisl, J. Universality in oxygen evolution electrocatalysis on oxide surfaces. *ChemCatChem* **2011**, 3, 1159.

(52) Lee, C. H.; Jun, B.; Lee, S. U. Metal-free oxygen evolution and oxygen reduction reaction bifunctional electrocatalyst in alkaline media: from mechanisms to structure-catalytic relationship. *ACS Sustainable Chem. Eng.* **2018**, 6, 4973-4980.

(53) Hammer, B.; Norskov, J. K. Why gold is the noblest of all the metals. *Nature* **1995**, 376, 238-240.

(54) Lee, J.; Yim, D.; Park, J. H.; Lee, C. H.; Ju, J.; Lee, S. U.; Kim, J. Tuning d-band centers by coupling PdO nanoclusters to WO_3 nanosheets to promote the oxygen reduction reaction. *J. Mater. Chem. A* **2020**, 8, 13490.

(55) Wagh, N. K.; Shine, S. S.; Lee, C. H.; Jung, J.; Kim, D.; Kim, S.; Lin, C.; Lee, S. U.; Lee, J. Densely colonized isolated Cu-N single sites for efficient bifunctional electrocatalysts and rechargeable advanced Zn-air batteries. *Appl. Catalysis B: Environ.* **2020**, 268, 118746.

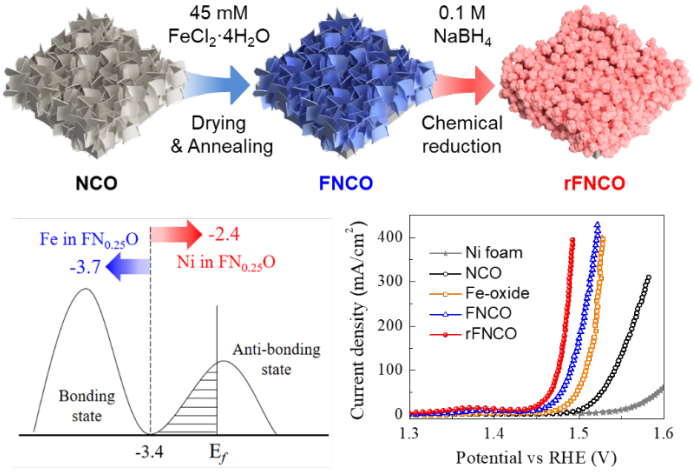
45 mM
$FeCl_2 \cdot 4H_2O$
Drying
& Annealing
0.1 M
$NaBH_4$
Chemical
reduction
NCO
FNCO
rFNCO
Fe in $FN_{0.25}O$
-3.7
-2.4
Ni in $FN_{0.25}O$
Anti-bonding
state
Bonding
state
-3.4
E_f
Ni foam
NCO
Fe-oxide
FNCO
rFNCO
Current density (mA/cm^2)
400
300
200
100
0
1.3
1.4
1.5
1.6
Potential vs RHE (V)